Geophysical Research Letters

RESEARCH LETTER
10.1029/2020GL087388

The Seasonality of Submesoscale Energy Production, Content, and Cascade

Jihai Dong[1,2], Baylor Fox-Kemper[3], Hong Zhang[4], and Changming Dong[1,2]

[1]School of Marine Sciences, Nanjing University of Information Science and Technology, Nanjing, Jiangsu, China, [2]Southern Marine Science and Engineering Guangdong Laboratory (Zhuhai), Zhuhai, Guangdong, China, [3]Department of Earth, Environmental and Planetary Sciences, Brown University, Providence, Rhode Island, USA, [4]Jet Propulsion Laboratory, California Institute of Technology, Pasadena, California, USA

Key Points:
- Strongest submesoscales in the Kuroshio Extension System occur in March with a month lag behind mixed layer thickness maximum in February
- The buoyancy production is in phase with the mixed layer depth, but the nonlinear transfers of energy across scales lag a few months behind
- The seasonality of the submesoscale energy is a result of the competition between the buoyancy production and nonlinear energy cascade

Supporting Information:
- Supporting Information S1

Correspondence to:
C. Dong,
cmdong@nuist.edu.cn

Citation:
Dong, J., Fox-Kemper, B., Zhang, H., & Dong, C. (2020). The seasonality of submesoscale energy production, content, and cascade. *Geophysical Research Letters*, *47*, e2020GL087388. https://doi.org/10.1029/2020GL087388

Received 6 FEB 2020
Accepted 12 MAR 2020
Accepted article online 13 MAR 2020

Abstract Submesoscale processes in the upper ocean vary seasonally, in tight correspondence with mixed layer thickness variability. Based on a global high-resolution MITgcm simulation, seasonal evaluation of strong vorticity and spectral analysis of the kinetic energy in the Kuroshio Extension System show the strongest submesoscales occur in March, implying a lag of about a month behind mixed layer thickness maximum in February. An analysis of spectral energy sources and transfers indicates that the seasonality of the submesoscale energy content is a result of the competition between the conversion of available potential energy into submesoscale kinetic energy via a buoyancy production/vertical buoyancy flux associated with mixed layer instability and nonlinear energy transfers to other scales associated with an energy cascade. The buoyancy production is seasonally in phase with the mixed layer depth, but the transfers of energy across scales makes energizing the reservoir of submesoscale kinetic energy lag behind by a month.

Plain Language Summary Submesoscale processes have spatial and temporal scales of O(1–10) km and O(1) day, linking the meso- and micro-scales. Previous works reveal that mixed layer instability, which has extraction rates scaled with mixed layer depth, releases potential energy for the generation of submesoscale kinetic energy in the upper ocean. However, the seasonality of submesoscale kinetic energy in the Kuroshio Extension System region is determined not only by the potential energy releasing due to the mixed layer instability, but also by the energy transfers between different scales.

1. Introduction

As the intermediate between meso- and micro-scales, submesoscale processes have a spatio-temporal scale of O(1–10) km and O(1) day (McWilliams, 2016; Thomas et al., 2008). Dynamically, submesoscales are defined to have Rossby and Richardson numbers that are order unity: $Ro \sim 1$, $Ri \sim 1$. Submesoscale processes make a significant contribution to the vertical ocean heat and material transports (Lévy et al., 2012; Su et al., 2018; Uchida et al., 2019), and occasionally significant horizontal transports (Capet et al., 2008; Pearson et al., 2019; Zhong et al., 2012).

Submesoscales can be generated by a number of mechanisms, including mixed layer instability (Boccaletti et al., 2007; Fox-Kemper et al., 2008), frontogenesis (Capet et al., 2008a; Hoskins, 1982; McWilliams, 2016), symmetric instability (Bennetts & Hoskins, 1979; Hoskins, 1974; Thomas et al., 2013), and topographic interactions (Gula et al., 2016). Mixed layer instability and strain-induced frontogenesis provide conversions of potential energy (PE) into ubiquitous submesoscale kinetic energy (KE) in the upper ocean mixed layer at a rate that scales with the mixed layer thickness squared (Fox-Kemper et al., 2008; McWilliams, 2016), while turbulent thermal wind frontogenesis rate is proportional to the mixed layer thickness (McWilliams, 2016). As a result, submesoscale processes have strong seasonal variability, tending to be more active in winter than summer, both from observation (Buckingham et al., 2016; Callies et al., 2015; Yu et al., 2019) and simulation (Dong & Zhong, 2018; Mensa et al., 2013; Rocha et al., 2016; Sasaki et al., 2017; Su et al., 2018), although important exceptions can be caused by seasonality in PE sources such as rivers (Barkan et al., 2017).

Three-dimensional turbulence transfers KE to smaller and smaller scales where it is ultimately dissipated (Kolmogorov, 1991); Two-dimensional and quasi-geostrophic theory predicts an inverse cascade in the

inertial range above the scales at which baroclinic instability converts available PE to KE and a downscale enstrophy cascade below (Charney, 1971; Kraichnan, 1967). However, submesoscale processes are not isotropically three-dimensional, nor purely two-dimensional or quasi-geostrophic due to the moderate symmetry-breaking effects of rotation and stratification implied by order one Rossby and Richardson numbers. Many studies have demonstrated a significant role of submesoscales in ocean energy cascade after Capet et al. (2008b). The contribution to inverse and forward energy cascades from submesoscales is studied successively in different regions based on high-resolution observations and simulations, such as the subtropical North Pacific (Qiu et al., 2014), Drake Passage (Rocha et al., 2016), Kuroshio extension (Sasaki et al., 2017), South Indian Ocean (Schubert et al., 2019) and South China Sea (Zhang et al., 2016; Zhang et al., 2020). All of these works emphasize the importance of submesoscales in the ocean energy cascade, and some use the same model simulations analyzed in this study.

In this work, the seasonality of submesoscale processes in the Kuroshio Extension System (KES) region is investigated based on a high-resolution global model simulation (MITgcm LLC4320). The seasonality of KE cannot be explained simply by the variations in the rate of PE released associated with the mixed layer depth variations. Instead, the contribution of the energy cascade to the submesoscale seasonality is also required and emphasized in this study. The paper is organized as follows: Section 2 introduces the model output and methods that used here; Section 3 describes the submesoscale seasonality in the KES, and discusses the mechanism that modulates the seasonality; the last section summarizes the work.

2. Model and Methods

2.1. Model Description

The model simulation analyzed is the Massachussetts Institute of Technology general circulation model (MITgcm) on a Latitude-Longitude polar Cap (LLC) grid (Forget et al., 2015; Menemenlis et al., 2008; Rocha, Chereskin, et al., 2016; Rocha, Gille, et al., 2016). The model simulation is named as LLC4320, which has a horizontal resolution of 1/48° with 90 vertical layers over the globe. The model is forced by six-hourly atmospheric forcings from the 0.14° European Centre for Medium-Range Weather Forecasting and 16 most significant tidal constituents. The vertical mixing is accomplished by using the K-profile Parameterization (KPP). The initial model state was derived from a 1/6° global ocean state estimate generated by the Estimating the Circulation and Climate of the Ocean (ECCO), Phase II project, and then a set of simulations were successively developed with increasing resolution of 1/12°, 1/24° and finally 1/48°. The LLC4320 is simulated for 14 months, from Sep 2011 to November 2012. The essential model states are stored at hourly snapshot.

This model's output has been widely applied, especially for studying submesoscale processes (e.g., Rocha, Chereskin, et al., 2016; Rocha, Gille, et al., 2016; Su et al., 2018; Viglione et al., 2018). The work by Rocha, Gille, et al. (2016) is of special note as inspiration for this study as it focuses on the submesoscale seasonality in the KES region, and demonstrates that the upper ocean density structure and eddy KE are well captured by this model simulation.

2.2. Temporal and Spatial Filtering

The barotropic tides in the model can generate strong internal waves under the interaction with topography. And the high-frequency wind forcing can also generate inertial internal waves. These internal waves have a spatial scale similar to the submesoscale currents, which potentially impacts the analysis result. Hence, the velocity and tracer (temperature, salinity) fields in KES region are firstly filtered by using a temporal lowpass filter with a cutoff period of 30 hours. The period is little larger than that of the local near-inertial internal waves in the KES region, ensuring that most internal waves are excluded. Then submesoscales are extracted by using a spatial highpass filter. Here, the cutoff scale for the filtering is chosen to be 80 km based on a correlation analysis of the unfiltered variability identifying submesoscales, which will be explained in the next section.

2.3. The Spectral Kinetic Energy Balance

The application of a horizontal spatial Fourier transform to the primitive kinematic equation yields spectral KE balance equation (Capet, McWilliams, et al., 2008b),

$$\frac{\partial \mathrm{KE(k)}}{\partial \mathrm{t}} = \mathrm{ADV(k)} + \mathrm{PK(k)} + \mathrm{Res(k)}. \quad (1)$$

Here, the kinetic energy $KE(k) = \widehat{\boldsymbol{u}}^{*}\widehat{\boldsymbol{u}}\cdot k$, the advective spectral flux $ADV(k) = -\widehat{\boldsymbol{u}}^{*}\cdot(\widehat{\boldsymbol{u}\cdot\nabla})\boldsymbol{u}\cdot k$, and the production from PE or vertical buoyancy flux $PK(k) = \widehat{w}^{*}\widehat{b}\cdot k$ are the critical terms to analyze to understand the seasonality of KE. The 3D velocity is $\boldsymbol{u}$, w is the vertical component of velocity, b is the buoyancy defined as $-g\frac{\rho}{\overline{\rho}}$, k is the wavenumber interval corresponding to the horizontal resolution. The caret denotes a horizontal spatial Fourier transform after removing the areal mean and asterisk denotes complex conjugate. The residual $Res(k)$ includes pressure work, horizontal and vertical dissipation, and is small and so will be not discussed here. The wind work in $Res(k)$ is an important energy source for ocean KE, and demonstrated to be able to interact with submesoscales (McWilliams, 2016; Renault et al., 2019; Thomas & Lee, 2005). A rough evaluation using daily snapshots of this contribution is made in this model and is found to be two orders of magnitude smaller than other terms in the energy budget. Thus, a more accurate evaluation is unlikely to show this effect changes the storyline here, and in any case we are unable to do the evaluation of wind-work at high-frequency based on what fields are saved of the LLC4320 results. Actually, $Res(k)$ is beyond the scope of this paper, as the submesoscale seasonality is explained fully by the other two terms. Only the real part is considered in the expression, so all phases in space (and time) are co-located (and simultaneous). Equation (1) provides the rate of change of KE density at a given wavenumber, which is mostly determined by the combined effects of the advective spectral flux and production. The advective spectral flux underlies the energy cascade and transfers energy conservatively between different scales, while the production or vertical buoyancy flux transforms available PE to KE.

3. Seasonality of Submesoscale Processes

3.1. Seasonal Variability

Submesoscale processes tend to have a significant ageostrophic component with $Ro \sim 1$, so following Rocha, Gille, et al. (2016) the normalized vertical vorticity (ζ/f, $\zeta = v_x - u_y$, f is the local planetary vorticity) is a good indicator for the submesoscale activity, and can be regarded as the Rossby number. A magnitude in this ratio near unity implies submesoscale processes. The Rossby number at the sea surface calculated based on the original velocity field at different times shows the spatial distribution of submesoscale processes in the northwest Pacific Ocean (Figure 1a, b). The Rossby number is generally relative weak in September in this simulation, and only few submesoscale filaments and eddies can be observed in the KES region. In contrast, the Rossby number is enhanced remarkably with magnitude up to 1.5 including ubiquitous submesoscale filaments and eddies, especially in the KES and subtropical regions. Zooming into rectangular regions shows more detailed vortical structures (Figure 1c, d). Stronger submesoscale filaments and eddies are found in March than September. Positive vorticity is stronger than the negative, as large anticyclonic vorticities (i.e. $\zeta/f < -1$) are quickly destroyed by inertial instability (Capet et al., 2008c; Shcherbina et al., 2013).

The vorticity derived from the original unfiltered velocity field also shows stripes and patches, in addition to the submesoscale filaments and eddies (such as close to the Japanese archipelago and subtropical region in Figure 1c). These features are more obvious in September compared with March and are attributed to the inertial-gravity waves (Rocha, Gille, et al., 2016). The enhanced stratification in summer favors the generation of internal waves. The application of a 30-hr temporal lowpass filter (Figure 1e, f) greatly diminishes these features. Previous works have applied a daily-averaging method to remove internal waves (Rocha, Gille, et al., 2016; Su et al., 2018). However, the lowpass filtering method is chosen here to retain submesoscale energy to a larger extent than with daily averaging.

Based on the lowpass filtered velocity field, the probability of the Rossby number larger than 0.8 ($|\zeta/f| > 0.8$, an indicator for the submesoscale activity) in different months from September 2011 to August 2012 is calculated (blue line in Figure 2a). The Rossby number probability has a strong seasonal variability with a peak in March. The probability variation indicates the submesoscales are more active in winter, which is consistent with the root mean square variation of vertical vorticity from the works of Rocha, Gille, et al. (2016) and Sasaki et al. (2017). This seasonality is usually attributed to more PE storage due to a deeper mixed layer depth in winter. The mixed layer depth derived from the model simulation is thick in winter up to 140 m,

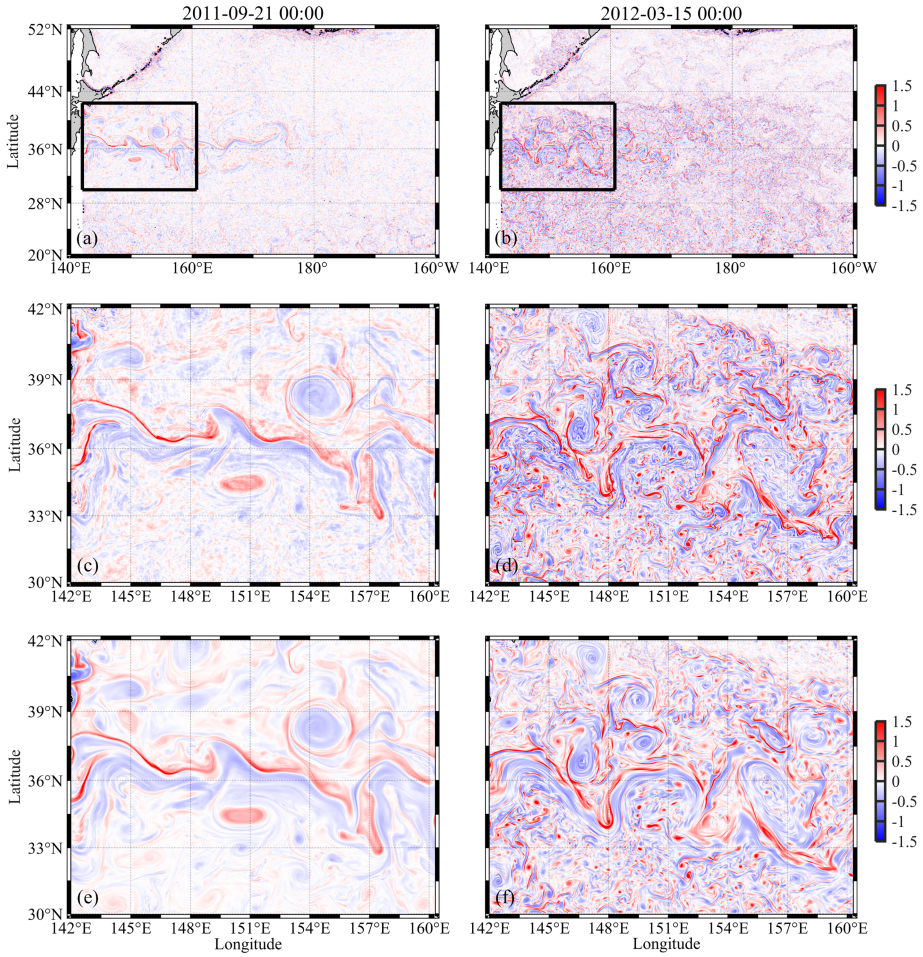

Figure 1. The instantaneous spatial distributions of the vertical relative vorticity (normalized by the local planetary vorticity, *f*, i.e., Rossby number) at the sea surface on 21 September 2011 (left column) and 15 march 2012 (right column). The distributions of the Rossby number calculated from the original velocity filed are shown in (a, b). The middle and lower panels show the distributions in the region denoted by the black rectangles. The Rossby number in (c, d) is calculated from the original velocity field, while (e, f) from the temporal lowpass filtered velocity filed.

but shallow in summer—often less than 10 m (blue line in Figure 2b). The Rossby number probability and mixed layer depth show a good consistency in seasonality.

However, the Rossby number probability and submesoscale KE occur somewhat after the mixed layer depth thickens and the production term energizes. The mixed layer depth peaks in February, a month earlier than the probability. The lag of the vorticity peak can be noted as well in Rocha, Gille, et al. (2016) and Sasaki et al. (2017). Corresponding with the probability, the submesoscale energy with scales below 80 km is isolated based on spatial highpass filtering to make the correlation maximal between the submesoscale KE ($KE = \rho\frac{u'^2+v'^2}{2}$, u' and v' are the submesoscale zonal and meridional velocities after spatial highpass filtering) and the Rossby number probability (red line in Figure 2a). After this filter-based definition (spatial highpass at 80 km, temporal lowpass at 30 hr) is applied, the maximum submesoscale KE in winter is 5 times larger than in summer. The PE production or vertical buoyancy flux is calculated as the average of the product of the analogous submesoscale vertical velocity w' and buoyancy perturbation b' ($b' = -g\frac{\rho'}{\overline{\rho}}$) obtained using the same spatial filter scale of 80 km and temporal filter scale of 30 hr. This covariance is the physical space equivalent to *PK* in spectral space in Equation 1. The monthly-averaged vertical buoyancy flux at 25 m depth is shown (red line in Figure 2b). It is almost zero in summer and largest in winter. The buoyancy flux corresponds in phase with the mixed layer depth, peaking in February, one month ahead of the Rossby

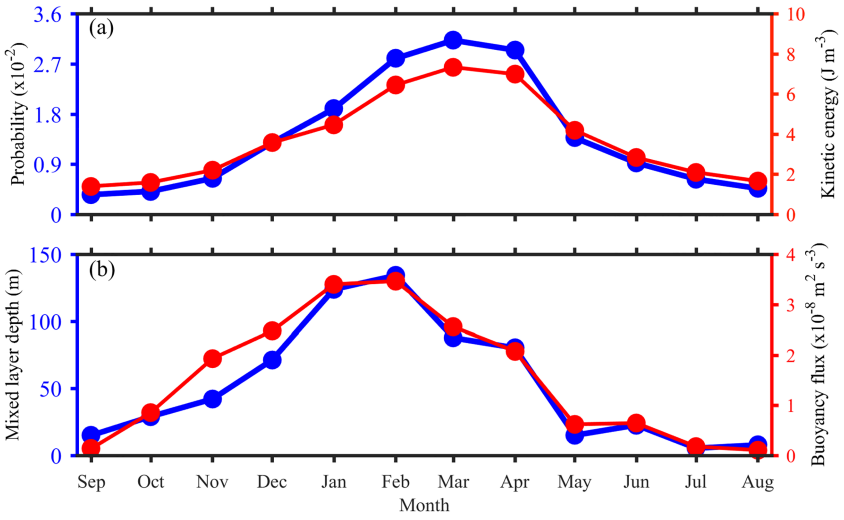

Figure 2. The monthly time series of a the probability of the Rossby number with value larger than 0.8 ($|\zeta/f| > 0.8$, blue line) at surface, the KE from spatial scales below 80 km (red line) at surface, b mixed layer depth derived from the model simulation (blue line), the vertical buoyancy flux below spatial scale 80 km at 25 m depth (red line). The mixed layer depth is defined as the depth where the density increase compared to density at surface corresponds to a temperature decrease of 0.2 °C in local surface conditions (de Boyer Montégut et al., 2004).

number probability and submesoscale KE. The mean buoyancy flux is always positive, so it tends to make the submesoscale KE increase at all times. As a result, the peak of Rossby number probability and submesoscale KE cannot be explained solely by the buoyancy flux.

3.2. Mixed Layer Instability Vs. Energy Cascade

As shown by Equation 1, another term that affects the submesoscale KE is the energy transfer between scales, namely, advective spectral flux. Both terms, *PK* and *ADV*, are calculated along horizontal wavenumber in Figure 3. *ADV* and *PK* are strong in the small wavenumber range, 1x10^{-6}~1x10^{-5} cycles m^{-1}

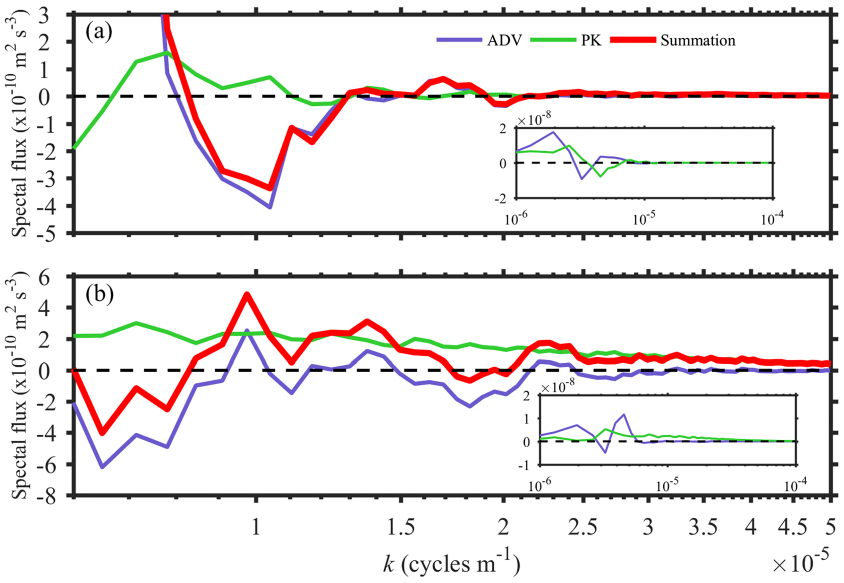

Figure 3. The depth-averaged spectral fluxes over the submesoscale range in the upper 50 m versus horizontal wavenumber in a September and b February. The nonlinear advective spectral flux (blue), *ADV*, vertical buoyancy flux (green), *PK* and their summation (red) are shown. The inserted subpanels show the spectral fluxes in a wider wavenumber range including the mesoscale and approaching the Nyquist scale (*PK* is amplified by 10 times in the subpanels).

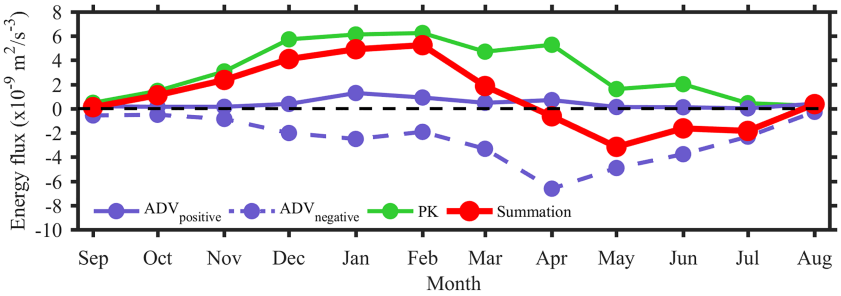

Figure 4. The monthly energy fluxes integrated along the wavenumber above 1.25x10^{-5} cycles m^{-1} (below 80 km). The integration from positive *ADV*, negative *ADV*, *PK* and summation denoted by blue solid, blue dashed, green and red lines, respectively.

(corresponding to large horizontal scale of 100~1000 km) and weak in large wavenumber (below 100 km; subpanels in Figure 3). *ADV* is generally larger than *PK*, since *PK* is amplified by 10 times in the subpanels for comparison. However, *ADV* and *PK* become comparable in wavenumber larger than 1x10^{-5} cycles m^{-1} (below 100 km).

PK is weaker in September compared with *ADV* (Figure 3a). The generally positive *PK* still implies the positive contribution of *PK* to the KE change. The weak *PK* in summer has been revealed in the preceding section (Figure 2b). In contrast, *ADV* is much stronger and large negative value can be observed especially around the scale of 100 km, which indicates that the advective spectral flux transfers KE to larger scales, i.e., inverse cascade. But as the wavenumber increases to about 1.7x10^{-5} cycles m^{-1} (about 60 km), weakly positive *ADV* increases the KE at that scale. Overall, the summation of these two terms is dominated by *ADV*.

The circumstance becomes quite different in winter when submesoscales are active (Figure 3b). On one hand, *PK* is enhanced remarkably in the submesoscale range indicating conversion of PE into KE, as is *ADV* indicating transfer of KE across scales. The strong positive *PK* provides the energy source for the generation of submesoscales. On the other hand, *ADV* becomes more complicated due to the variety of submesoscale processes combining with mesoscale processes. The strong negative *ADV* on scales with wavenumber larger than 0.9x10^{-5} cycles m^{-1} (>110 km) and between 1.5x10^{-5} ~ 2.3x10^{-5} cycles m^{-1} (45 ~ 65 km) moves energy toward smaller wavenumbers (larger scales), which is more complicated compared with that in summer. The positive *ADV* is enhanced (note different vertical axis scales) and strong positive *ADV* is scattered across the wavenumber range of 1x10^{-5} ~ 1.5x10^{-5} cycles m^{-1} (65 ~ 100 km). The summation of *ADV* and *PK* leads to a generally positive spectral flux in the submesoscale range 8x10^{-6} ~ 4x10^{-5} cycles m^{-1} (25 ~ 125 km), indicating an increasing tendency of KE across these scales. The positive *ADV* in winter associated with active submesoscales implies a forward energy cascade in submesoscale range, especially at smaller scale, potentially contributing to local mixing (Capet, McWilliams, et al., 2008b; Yang et al., 2017).

The energy fluxes integrated from the spectral fluxes of *PK* and *ADV* on wavenumbers larger than 1.25x10^{-5} cycles m^{-1} (80 km length scale) are investigated, since the submesoscale KE below 80 km was identified to correlate with the Rossby number probability (Figure 4). The integrated energy fluxes indicate the contributions from these two terms to the KE in the submesoscale range. The energy conversion from potential to KE integrated from *PK* over the submesoscale has an obvious seasonal variability and peaks in February, which is consistent with that calculated directly from the physical space estimate (green line in Figure 4) and this timing coincides with the deepest seasonal mixed layers. The spectrally integrated value is smaller than the physical estimate, since it is an average over a wider depth range. The integration of *ADV* (blue lines in Figure 4) is divided into two parts, the integral over wavenumbers with positive *ADV* (scales to which energy is delivered) and those with negative *ADV* (scales from which energy is extracted). The positive contribution is enhanced in winter, indicating that submesoscale processes receive KE via nonlinear interactions. The negative contribution of *ADV* peaks in April, lagging behind the peak of the positive contribution slightly. Overall, the negative *ADV* dominates the positive contribution, so the submesoscale

acts to energize other length scales (e.g., Callies et al., 2016), supporting an inverse energy cascade transferring energy from submesoscales to larger scales. As a result, the submesoscales lose energy due to the nonlinear advective spectral flux, but this withdrawal occurs after a few months' delay behind the production of submesoscale KE from PE.

The summation of the integrated *ADV* and *PK* shows a transition between positive submesoscale energy tendency and negative submesoscale energy decline due to the positive *PK* and negative *ADV* (red line in Figure 4). The total source is positive from September to March, steadily increasing over the seasons of mixed layer deepening from September to February and then decreasing as the production drops off during springtime re-stratification. From April to August, the already energized submesoscale begins to lose energy as the total becomes a negative sink that peaks in May, and then decreases to null in August. The seasonality of the total flux indicates that submesoscale processes obtain energy from September to March, but lose energy after April. Hence, the seasonality and peak of submesoscale activity in March is a result of the competition between sources and sinks of submesoscale energy, and because the sinks lag behind production, the maximum submesoscale energy content occurs after the maximum of production which coincides with the deepest mixed layers (Figure 2), but before the season of maximum energy transfer to larger scales (Figure 4).

4. Conclusions and Discussion

The seasonal variability is an important dynamic feature of submesoscale processes, which implies potential generation mechanisms. The seasonal variability has been attributed to the vertical buoyancy flux and mixed layer thickness variability (Callies et al., 2015; Mensa et al., 2013; Sasaki et al., 2017). However, buoyancy flux variability fails to explain the submesoscale energy seasonality completely, since the buoyancy flux is always positive (i.e., re-stratifying and extracting PE) in the submesoscale range. The sinks of submesoscale energy are an important consideration, and this work shows that they may be dominated by advective transfer to larger scales which may lag a few months behind the production of energy. In the KES study region, the submesoscale activity (high Rossby number probability and strong submesoscale energy) peaks in March, a month behind the vertical buoyancy flux and mixed layer thickness which peak in February.

Recently, a variety of parameterizations of eddies based on energy content have been proposed (e.g., Bachman et al., 2017; Jansen et al., 2019). Here it is important to note that the re-stratification effect, which is parameterized in Fox-Kemper et al. (2008, 2011) is not temporally coincident with the submesoscale energy content, indicating that a deeper analysis of these effects is needed. It may be that distinguishing lateral transport from vertical re-stratification as a function of time is needed to explain both phenomena consistently.

In this work, a 1-month lag is found between the submesoscale activity and mixed layer depth. However, the correlation between the submesoscale activity and mixed layer depth varies regionally. Examining a broader swath of the North Pacific Ocean, submesoscale energy and vorticity tends to lag production in most regions, but an in-phase correlation occurs in the Subarctic Western Pacific region (Figure 6 of Sasaki et al., 2017). Mensa et al. (2013) in the Gulf Stream also find a lagged correlation (Figure 18 of Mensa et al., 2013). The submesoscale activity peak is determined by the time of sign reversal of the net energy tendency, which in this analysis mainly depends on the seasonality of the *ADV*. One possible explanation for the lag of the negative *ADV* peak behind the *PK* peak is the seasonal strength difference between submesoscales and larger scales (above 80 km). The larger scale KE is stronger in summer while submesoscale energy is accumulated in winter (Figure S1 in the supporting information; e.g., Sasaki et al., 2017). The remarkable increase of the relative energy content of larger scales in spring affects the nonlinear interactions between submesoscales and larger scales, manifested in the inverse cascade and weakening submesoscales. So, the negative *ADV* is inferred to be strong in spring, but relatively weak at other times of year. Other sources and sinks of energy, such as riverine inputs of PE (Barkan et al., 2017), bottom drag or topographic interactions in shelf seas (Gula et al., 2016), and possibly forward energy cascades under other forcing conditions (Capet, McWilliams, et al., 2008b) will lead to other distinct regimes of energetic seasonality. In any case, sinks of submesoscale energy should be considered alongside sources since the conversion of PE by vertical buoyancy flux and re-stratification does not reduce the submesoscale KE.

Acknowledgments

This work is supported by National Key Research Program of China (2017YFA0604100). JHD acknowledges support from and the National Natural Science Foundation of China (41806025) and the China Scholarship Council. BFK acknowledges support from the National Key Research Program of China (2017YFA0604100), NSF OCE-1350795, and ONR N00014-17-1-2963. The Authors wish to thank the ECCO team (https://ecco.jpl.nasa.gov) for development and production of LLC4320 simulation. The LLC4320 data can be directly accessed from ECCO Data Portal (https://data.nas.nasa.gov/ecco/data.php), or more conveniently downloaded by using the xmitgcm python package (https://xmitgcm.readthedocs.io/en/latest/index.html).

References

Bachman, S. D., Marshall, D. P., Maddison, J. R., & Mak, J. (2017). Evaluation of a scalar eddy transport coefficient based on geometric constraints. *Ocean Modelling*, *109*, 44–54. https://doi.org/10.1016/j.ocemod.2016.12.004

Barkan, R., McWilliams, J. C., Shchepetkin, A. F., Molemaker, M. J., Renault, L., Bracco, A., & Choi, J. (2017). Submesoscale dynamics in the northern Gulf of Mexico. Part I: Regional and seasonal characterization and the role of river outflow. *Journal of Physical Oceanography*, *47*(9), 2325–2346. https://doi.org/10.1175/jpo-d-17-0035.1

Bennetts, D. A., & Hoskins, B. J. (1979). Conditional symmetric instability-a possible explanation for frontal rainbands. *Quarterly Journal of the Royal Meteorological Society*, *105*(446), 945–962. https://doi.org/10.1002/qj.49710544615

Boccaletti, G., Ferrari, R., & Fox-Kemper, B. (2007). Mixed layer instabilities and restratification. *Journal of Physical Oceanography*, *37*(9), 2228–2250. https://doi.org/10.1175/jpo3101.1

Buckingham, C. E., Naveira Garabato, A. C., Thompson, A. F., Brannigan, L., Lazar, A., Marshall, D. P., et al. (2016). Seasonality of submesoscale flows in the ocean surface boundary layer. *Geophysical Research Letters*, *43*, 2118–2126. https://doi.org/10.1002/2016gl068009

Callies, J., Ferrari, R., Klymak, J. M., & Gula, J. (2015). Seasonality in submesoscale turbulence. *Nature Communications*, *6*, 6862. https://doi.org/10.1038/ncomms7862

Callies, J., Flierl, G., Ferrari, R., & Fox-Kemper, B. (2016). The role of mixed-layer instabilities in submesoscale turbulence. *Journal of Fluid Mechanics*, *788*, 5–41. https://doi.org/10.1017/jfm.2015.700

Capet, X., Campos, E. J., & Paiva, A. M. (2008). Submesoscale activity over the Argentinian shelf. *Geophysical Research Letters*, *35*, L15605. https://doi.org/10.1029/2008gl034736

Capet, X., McWilliams, J. C., Molemaker, M. J., & Shchepetkin, A. (2008a). Mesoscale to submesoscale transition in the California current system. Part II: Frontal processes. *Journal of Physical Oceanography*, *38*(1), 44–64. https://doi.org/10.1175/2007jpo3672.1

Capet, X., McWilliams, J. C., Molemaker, M. J., & Shchepetkin, A. (2008b). Mesoscale to submesoscale transition in the California current system. Part III: Energy balance and flux. *Journal of Physical Oceanography*, *38*(10), 2256–2269. https://doi.org/10.1175/2008jpo3810.1

Capet, X., McWilliams, J. C., Molemaker, M. J., & Shchepetkin, A. (2008c). Mesoscale to submesoscale transition in the California current system. Part I: Flow structure, eddy flux, and observational tests. *Journal of Physical Oceanography*, *38*(1), 29–43. https://doi.org/10.1175/2007jpo3671.1

Charney, J. G. (1971). Geostrophic turbulence. *Journal of the Atmospheric Sciences*, *28*(6), 1087–1095. https://doi.org/10.1175/1520-0469(1971)028<1087:GT>2.0.CO;2

de Boyer Montégut, C., Madec, G., Fischer, A. S., Lazar, A., & Iudicone, D. (2004). Mixed layer depth over the global ocean: An examination of profile data and a profile-based climatology. *Journal Geophysical Research*, *109*, C12003. https://doi.org/10.1029/2004JC002378

Dong, J., & Zhong, Y. (2018). The spatiotemporal features of submesoscale processes in the northeastern South China Sea. *Acta Oceanologica Sinica*, *37*(11), 8–18. https://doi.org/10.1007/s13131-018-1277-2

Forget, G., Campin, J.-M., Heimbach, P., Hill, C. N., Ponte, R. M., & Wunsch, C. (2015). ECCO version 4: An integrated framework for non-linear inverse modeling and global ocean state estimation. *Geoscientific Model Development*, *8*(10). https://doi.org/10.5194/gmd-8-3071-2015

Fox-Kemper, B., Danabasoglu, G., Ferrari, R., Griffies, S. M., Hallberg, R. W., Holland, M. M., et al. (2011). Parameterization of mixed layer eddies. III: Implementation and impact in global ocean climate simulations. *Ocean Modelling*, *39*(1–2), 61–78. https://doi.org/10.1175/jpo-d-17-0035.1

Fox-Kemper, B., Ferrari, R., & Hallberg, R. (2008). Parameterization of mixed layer eddies. Part I: Theory and diagnosis. *Journal of Physical Oceanography*, *38*(6), 1145–1165. https://doi.org/10.1175/2007jpo3792.1

Gula, J., Molemaker, M. J., & McWilliams, J. C. (2016). Topographic generation of submesoscale centrifugal instability and energy dissipation. *Nature Communications*, *7*, 12,811. https://doi.org/10.1016/j.ocemod.2010.09.002

Hoskins, B. (1982). The mathematical theory of frontogenesis. *Annual Review of Fluid Mechanics*, *14*(1), 131–151. https://doi.org/10.1146/annurev.fl.14.010182.001023

Hoskins, B. J. (1974). The role of potential vorticity in symmetric stability and instability. *Quarterly Journal of the Royal Meteorological Society*, *100*(425), 480–482. https://doi.org/10.1002/qj.49710042520

Jansen, M. F., Adcroft, A., Khani, S., & Kong, H. (2019). Towards an energetically consistent, resolution aware parameterization of ocean mesoscale eddies. *Journal of Advances in Modeling Earth Systems*, *11*(8), 2844–2860. https://doi.org/10.1029/2019ms001750

Kolmogorov, A. N. (1991). Dissipation of energy in locally isotropic turbulence. *Proceedings of the Royal Society A: Mathematical, Physical*, *32*, 16. https://doi.org/10.1098/rspa.1991.0076

Kraichnan, R. H. (1967). Inertial ranges in two-dimensional turbulence. *Physics of Fluids*, *10*(7), 1417–1423. https://doi.org/10.1063/1.1762301

Lévy, M., Ferrari, R., Franks, P. J., Martin, A. P., & Rivière, P. (2012). Bringing physics to life at the submesoscale. *Geophysical Research Letters*, *39*, L14602. https://doi.org/10.1029/2012gl052756

McWilliams, J. C. (2016). Submesoscale currents in the ocean. *Proceedings of the Royal Society A: Mathematical, Physical and Engineering Sciences*, *472*(2189). https://doi.org/10.1098/rspa.2016.0117

Menemenlis, D., Campin, J.-M., Heimbach, P., Hill, C., Lee, T., Nguyen, A., et al. (2008). ECCO2: High resolution global ocean and sea ice data synthesis. *Mercator Ocean Quarterly Newsletter*, *31*(October), 13–21.

Mensa, J. A., Garraffo, Z., Griffa, A., Özgökmen, T. M., Haza, A., & Veneziani, M. (2013). Seasonality of the submesoscale dynamics in the Gulf stream region. *Ocean Dynamics*, *63*(8), 923–941. https://doi.org/10.1007/s10236-013-0633-1

Pearson, J., Fox-Kemper, B., Barkan, R., Choi, J., Bracco, A., & McWilliams, J. C. (2019). Impacts of convergence on structure functions from surface drifters in the Gulf of Mexico. *Journal of Physical Oceanography*, *49*(3), 675–690. https://doi.org/10.1175/jpo-d-18-0029.1

Qiu, B., Chen, S., Klein, P., Sasaki, H., & Sasai, Y. (2014). Seasonal mesoscale and submesoscale eddy variability along the North Pacific subtropical Countercurrent. *Journal of Physical Oceanography*, *44*(12), 3079–3098. https://doi.org/10.1175/jpo-d-14-0071.1

Renault, L., Marchesiello, P., Masson, S., & Mcwilliams, J. C. (2019). Remarkable control of western boundary currents by eddy killing, a mechanical air-sea coupling process. *Geophysical Research Letters*, *46*(5), 2743–2751. https://doi.org/10.1029/2018GL081211

Rocha, C. B., Chereskin, T. K., Gille, S. T., & Menemenlis, D. (2016). Mesoscale to submesoscale wavenumber spectra in Drake Passage. *Journal of Physical Oceanography*, *46*(2), 601–620. https://doi.org/10.1175/jpo-d-15-0087.1

Rocha, C. B., Gille, S. T., Chereskin, T. K., & Menemenlis, D. (2016). Seasonality of submesoscale dynamics in the Kuroshio extension. *Geophysical Research Letters*, *43*, 11,304–311,311. https://doi.org/10.1002/2016gl071349

Sasaki, H., Klein, P., Sasai, Y., & Qiu, B. (2017). Regionality and seasonality of submesoscale and mesoscale turbulence in the North Pacific Ocean. *Ocean Dynamics*, *67*(9), 1195–1216. https://doi.org/10.1007/s10236-017-1083-y

Schubert, R., Schwarzkopf, F. U., Baschek, B., & Biastoch, A. (2019). Submesoscale impacts on mesoscale Agulhas dynamics. *Journal of Advances in Modeling Earth Systems*, *11*(8), 2745–2767. https://doi.org/10.1029/2019MS001724

Shcherbina, A. Y., D'Asaro, E. A., Lee, C. M., Klymak, J. M., Molemaker, M. J., & McWilliams, J. C. (2013). Statistics of vertical vorticity, divergence, and strain in a developed submesoscale turbulence field. *Geophysical Research Letters*, *40*, 4706–4711. https://doi.org/10.1002/grl.50919

Su, Z., Wang, J., Klein, P., Thompson, A. F., & Menemenlis, D. (2018). Ocean submesoscales as a key component of the global heat budget. *Nature Communications*, *9*(1), 775. https://doi.org/10.1038/s41467-018-02983-w

Thomas, L. N., & Lee, C. M. (2005). Intensification of ocean fronts by down-front winds. *Journal of Physical Oceanography*, *35*(6), 1086–1102. https://doi.org/10.1175/jpo2737.1

Thomas, L. N., Tandon, A., & Mahadevan, A. (2008). Submesoscale processes and dynamics. *Ocean modeling in an Eddying Regime*, *177*, 17–38. https://doi.org/10.1029/177gm04

Thomas, L. N., Taylor, J. R., Ferrari, R., & Joyce, T. M. (2013). Symmetric instability in the Gulf stream. *Deep Sea Research Part II: Topical Studies in Oceanography*, *91*, 96–110. https://doi.org/10.1016/j.dsr2.2013.02.025

Uchida, T., Balwada, D., Abernathey, R., McKinley, G., Smith, S., & Levy, M. (2019). The contribution of submesoscale over mesoscale eddy iron transport in the open Southern Ocean. *Journal of Advances in Modeling Earth Systems*, *11*, 3934–3958. https://doi.org/10.31223/osf.io/xwb75

Viglione, G. A., Thompson, A. F., Flexas, M. M., Sprintall, J., & Swart, S. (2018). Abrupt transitions in submesoscale structure in southern drake passage: Glider observations and model results. *Journal of Physical Oceanography*, *48*(9), 2011–2027. https://doi.org/10.1175/jpo-d-17-0192.1

Yang, Q., Zhao, W., Liang, X., Dong, J., & Tian, J. (2017). Elevated mixing in the periphery of Mesoscale eddies in the South China Sea. *Journal of Physical Oceanography*, *47*(4), 895–907. https://doi.org/10.1175/jpo-d-16-0256.1

Yu, X., Naveira Garabato, A. C., Martin, A. P., Buckingham, C. E., Brannigan, L., & Su, Z. (2019). An annual cycle of submesoscale vertical flow and restratification in the upper ocean. *Journal of Physical Oceanography*, *49*(6), 1439–1461. https://doi.org/10.1175/jpo-d-18-0253.1

Zhang, Z., Tian, J., Qiu, B., Zhao, W., Chang, P., Wu, D., & Wan, X. (2016). Observed 3D structure, generation, and dissipation of oceanic mesoscale eddies in the South China Sea. *Scientific Reports*, *6*, 24349. https://doi.org/10.1038/srep24349

Zhang, Z., et al. (2020). Spatiotemporal characteristics and generation mechanisms of submesoscale currents in the northeastern South China Sea revealed by numerical simulations. *Journal of Geophysical Research: Oceans. 125*(2). https://doi.org/10.1029/2019JC015404

Zhong, Y., Bracco, A., & Villareal, T. A. (2012). Pattern formation at the ocean surface: Sargassum distribution and the role of the eddy field. *Limnology and Oceanography*, *2*(1), 12–27. https://doi.org/10.1215/21573689-1573372